Graphene-Based Flexible Sensors for Respiratory and Airflow Monitoring

Graphene-Based Flexible Sensors for Respiratory and Airflow Monitoring

Yanhua Song[†], Long Chen[†], Qianqian Yang[⊥], Guang Liu[†], Qiwen Yu[†], Xiaoya Xie[†], Chao Chen[§], Jun Liu[†], Guanqun Chao[‡]，Xing Chen[†]*, Ming-Wei Chang[#]*

[†] Department of Biomedical Engineering, Key Laboratory for Biomedical Engineering of Education Ministry of China, Zhejiang Provincial Key Laboratory of Cardio-Cerebral Vascular Detection Technology and Medical Effectiveness Appraisal, Zhejiang University, 310027, China

[⊥] State Key Laboratory of Fluid Power and Mechatronic Systems, School of Mechanical Engineering, Zhejiang University, 310027, China

[§] GuoZhen Health Technology Co., Ltd., Beijing, 102206, China

[‡]Zhejiang Sir Run Run Shaw Hospital, Department of Medicine, Zhejiang University, Hangzhou, Zhejiang, 310027, China

[#] University of Ulster, Belfast, Northern Ireland, BT15 1AP, UK

Corresponding Author

*Email: cnxingchen@zju.edu.cn; m.chang@ulster.ac.uk

Abstract

Flexible devices have been rapidly developed and applied in various applications. However, there have been few reports on printable graphene-based sensors with customized structures and properties capable of respiratory and airflow monitoring. In this study, a graphene-based flexible sensor with a conical microdot array (GSCA) made by the direct-ink writing (DIW) 3D printing method for real-time personal signals and air-coupled detection is reported. GSCA 3D structures with microdot features on the sensing layer can deliver a fast response of below 60 ms and improve sensitivity by 32.4% (26-78 kPa), 800% (78-102 kPa), and 600% (102-160 kPa) by adjusting the printing parameters. The sensor exhibits a low detection limit of 11.4 Pa and a large detection range with a linear sensitivity of 1.4 kPa-509 kPa. The spider legs-like micro/nanofibers between two adjacent microdots contribute to electron transport and airflow sensing. The results show the feasibility of the graphene-based sensor with dots to recognize air strength and direction for respiration and airflow. Further validation of the GSCA in real-time personal monitoring demonstrates the potential for multitasking wearable sensors.

Keywords: graphene; direct-ink writing; wearable electronic; microdot; airflow.

1. Introduction

Flexible sensors that can conformably attach to various irregular surfaces, such as human-computer interfaces, human skin, and textiles, without any property degradation have been of interest in recent years.[1] This is evidenced by increasing research and development efforts in their flexibility and stretchability, as compared to traditional rigid sensors.[2, 3] Flexible sensors with multiple functionalities have been widely applied in robotics,[4, 5] prosthetics,[6, 7] human-computer interfaces,[8] and wearable healthcare devices.[9-14] Recently, the rapid development of new sensing materials has contributed to significant progress in sensing devices with unique advantages, such as high sensitivity, fast response, large detection range, and high resolution, to meet practical application requirements and broaden the scope of applications in respiration and airflow monitoring.[15] Previous research improved resolution by developing complex 2D/3D structures, such as spheres, domes, walls, pyramids, vertical pillars, rods, sheets, etc.[12] However, in these practical applications, flexible sensors unavoidably require multi-step fabrication to ensure stability in complex working environments.

Three-dimensional printing (3DP) methods can now be customized to meet the complexity and challenges of desired requests and personalization.[16, 17] Direct-ink writing (DIW) is a versatile 3DP technique used to fabricate micro/nano constructs with high resolution, making it possible to achieve bespoke structures and properties.[18, 19] Graphene-based flexible sensors fabricated by DIW have been successfully used in energy storage and electrodes due to their high sensitivity, good compliance, and printability.[20-24] By utilizing the unique properties of graphene-based materials and the precision of DIW printing techniques, it is possible to fabricate sensors with improved sensitivity and response times, capable of detecting even small variations in airflow direction and strength. However, the development of printed wearable flexible devices capable of determining the strength and direction of airflow in three dimensions is rarely discussed. Such advances would have significant implications for the design and functionality of future wearable devices, including those used in healthcare, sports, and other fields.

In this study, we present a graphene-based flexible sensor for wearable respiration and airflow monitoring using a robust, cost-effective, and straightforward DIW approach. The DIW-fabricated flexible sensor was equipped with a conical microdot array to enhance the sensitivity for the detection of air direction and intensity. The graphene-based flexible sensor with a conical microdot array (GSCA) was composed of polyethylene oxide (PEO), graphene (G), and polyaniline (PANI). Polymeric PEO is an excellent candidate for its unique ability to reach high ion mobility, while graphene (G) is a promising material for human physical signal monitoring. PANI was added to strengthen the π-π conjugated attraction with G and improve conductivity and sensitivity.[25] The printability and processing parameters such as the concentration of PEO/PANI/G, extrusion rate, printing speed, and working distance were investigated, allowing customization of the shape and performance of printed sensors. The GSCA showed a low detection limit of 11.4 Pa and had two linear regions in the detection range of 1.4-509 kPa. The printed sensor with microdots improved sensor sensitivity by 32.4% (26-78 kPa), 800% (78-102 kPa), and 600% (102-160 kPa) compared to the sensor without microdots. Thus, it provided excellent perception to identify air direction and intensity. The fast response time of 60 ms enabled the GSCA to detect real-time human pulse waves and respiration. In practical application, the results demonstrated its potential to be used as a multitasking wearable sensor for human physical signal detection and could simultaneously monitor airflow and respiration.

2. Materials and Method

2.1 Materials

Polyethylene oxide (PEO, Mw = 900,000) was purchased from Huagao Fine Chemical Co., Ltd., China. Few-layer graphene (G, purity > 98%, thickness 2 nm) was obtained from Tanfeng Graphene Technology Co., Ltd., Suzhou, China. Polyaniline (PANI, Mw 50,000-60,000, purity > 98%, conductivity 7.5 S/cm) was obtained from Shanghai Macklin Biochemical Co., Ltd., China. Absolute ethyl alcohol (EtOH) was purchased from Sinopharm Chemical Reagent, China. Deionized water was produced by a Millipore Milli-Q Reference ultra-pure water purifier (USA). All chemicals and

components were used without further purification. The A and B agents of polydimethylsiloxane (PDMS, Sylgard 184) were provided by Dow Corning (USA). A common glass collector was used in printing filaments and sensing films.

2.2 Preparation of printable sensing ink

G (0-2.1 wt%) and PANI (1.1-5.1 wt%) powders were dispersed in a mixture of DI water and EtOH (volume ratio: 3:7). PEO (7.4-12.9 wt%) was added to the dispersion liquid and stirred (VELP ARE, Italy) for 5 hours. Subsequently, the printable ink was obtained by stirring the entire solution matrix for 12 hours at room temperature.

2.3 Preparation of PDMS ink

The A (base) and B (curing agent) components of PDMS were mixed at a weight ratio of 10:1. After stirring (VELP ARE, Italy) for 10 minutes, the mixed liquid was put into a vacuum oven (D2F-6020AF, Tianjin, China) to remove bubbles. PDMS ink used for packaging was obtained.

2.4 Fabrication of sensing filaments and microdots

The printable sensing ink, consisting of PEO/PANI/G/EtOH/DI water, was loaded into a 5 ml injector and extruded out of a metal needle with an inner/outer diameter of 0.61/0.91 mm using an extrusion system (KD Scientific KDS100, USA) as shown in Figure 1a. During parameters optimization and filament printing, each filament was stacked only once and every parameter was set at 5 levels. The flow rate was set at 0.5-2.5 ml/h, the working distance was set at 0-2 mm, and the speed of the platform in Figure 1b was set at 10-100 mm/s. The extruded ink could be customized in any pattern with the assistance of a three-axis motion platform under computer control. The motion range of the Z-axis in this study was set at 0-8 mm. The distance between two adjacent conical microdots was set at 500 μm. The height of the microdots was designed and controlled from 0 to 27 layers (0, 9, 18, and 27). After the conical microdots were printed, the entire sensing film with the conical microdots array was air-dried at room temperature for 8 hours. Two conductive wires were then connected to the rear side of the sensing film without microdots. Subsequently, PDMS was applied to the top and bottom sides of the sensing film. The entire sensing film with PDMS was cured in a vacuum oven (D2F-6020AF, Tianjin, China) at 60 ℃ for 2 hours, then allowed to cool

at room temperature for 8 hours, resulting in a flexible sensor with dimensions of 11 × 25 mm². For all electromechanical performance and application tests, sensors were prepared using a 10-layer orthogonal sensing film with a 27-layered microdot array.

2.5 Material and morphology characterization

The thicknesses of the sensing film were measured using a digital micrometer (NSCING, Hangzhou Chentong Materials Co. LTD, China). The diameter of the single filament was analyzed using optical pictures obtained by an optical microscope (OM, Phenix BMC503-ICCF, China) and ImageJ software (National Institutes of Health, USA). The resistance of a single filament was measured using a high-precision multi-meter (SDM3055X-E, China) at every 1 cm interval, and the average value was calculated. The morphology and structure of the printed sensing film with and without microdots were examined using a field-emission scanning electron microscopy (SEM, SU8010, Hitachi, Japan) at an acceleration voltage of 0.1-30 kV. Structures and morphologies of the 10-layered orthogonal sensing film dispensed with conical microdots of 9, 18, and 27 layers were also observed via SEM. The elements of microdots were investigated by energy-dispersive X-ray spectroscopy (EDS, Be4-U92) on SEM. Construct composition, interactions, and material stability were determined by Attenuated Total Reflected Infrared Fourier Transform Infrared Spectroscopy (ATR-FTIR, Thermo Scientific™ Nicolet™ iS50 FTIR, USA) at a resolution of 0.09 cm^{-1} (15-27,000 cm^{-1}).

2.6 Electrical and Electrochemical characterization

A material testing machine (Instron 34SC-05, Instron, USA) was used to apply forces on the graphene-based sensors. The electrical and electromechanical properties of sensors were evaluated by connecting two wiring electrodes of the electrochemical workstation (Chi660e, Chenhua, China) to both sides of the sensing film, and the current was monitored with and without external pressure.

To measure human physical signals, a GSCA was attached to the index finger or wrist using double-sided adhesive tape, and the outputs were recorded under a direct voltage supply of 0.5 V using the chi660e electrochemical workstation. During respiration

monitoring, the sensor was embedded into a mask, and the two wires of the sensor were connected to an electrochemical workstation to record real-time outputs.

To study the influences of airflow at different strengths and angles on GSCA, the strength and angles of airflow were controlled by a glass rotameter (LZB-6WAF, Yuming instrument, China) and an air tank, respectively. All animal experimental procedures were performed in accordance with the guidelines and protocols of the Animal Experimental Ethics Committee of Zhejiang University (18156).

2.7 Sensitivity (S) calculation

$$S = \frac{\Delta R/R_0}{\Delta P} \times 100\%, \text{or } S = \frac{\Delta I/I_0}{\Delta P} \times 100\% \quad (1)$$

Where ΔR and ΔI represent the relative changes in resistance and current, respectively, with and without pressure applied separately. R_0 and I_0 are the initial resistance and current values of the sensing layer without pressure stimuli. ΔP represents the change in applied pressure.

3. Results and discussion

3.1 Evaluation of process parameters

Figure 1c shows that when printing parallel filaments in a single direction, the distance between two adjacent filaments was set at 68 μm (blue line segment), and each filament was stacked ten times. By controlling the position of the Z-axis and the directions of both the X and Y-axes, a sensing film of 10 layered filaments with printed conic microdots could be developed (Figure 1d). To explore the influence of processing parameters on the sensing properties of printed layers, the change in resistance and diameter of a single filament was measured. Figure 1e shows that the conductivity of the printed filament slightly reduced while the diameter decreased obviously with an increase in PEO concentration. Figure 1f indicates that the diameter of the printed filament increased owing to a large volume of G powders. The resistance decreased sharply and then reached a plateau when the G concentration was increased from 0 to 2.1 wt%. Figure 1g shows that the resistance curve had a reverse trend at a PANI concentration of 3.1 wt%, while the diameter elevated when PANI concentration

increased. When the concentration of PANI was over 3.1 wt%, the filament broke easily because of a high volume of powder, which resulted in lower conductivity and poor mechanical properties.

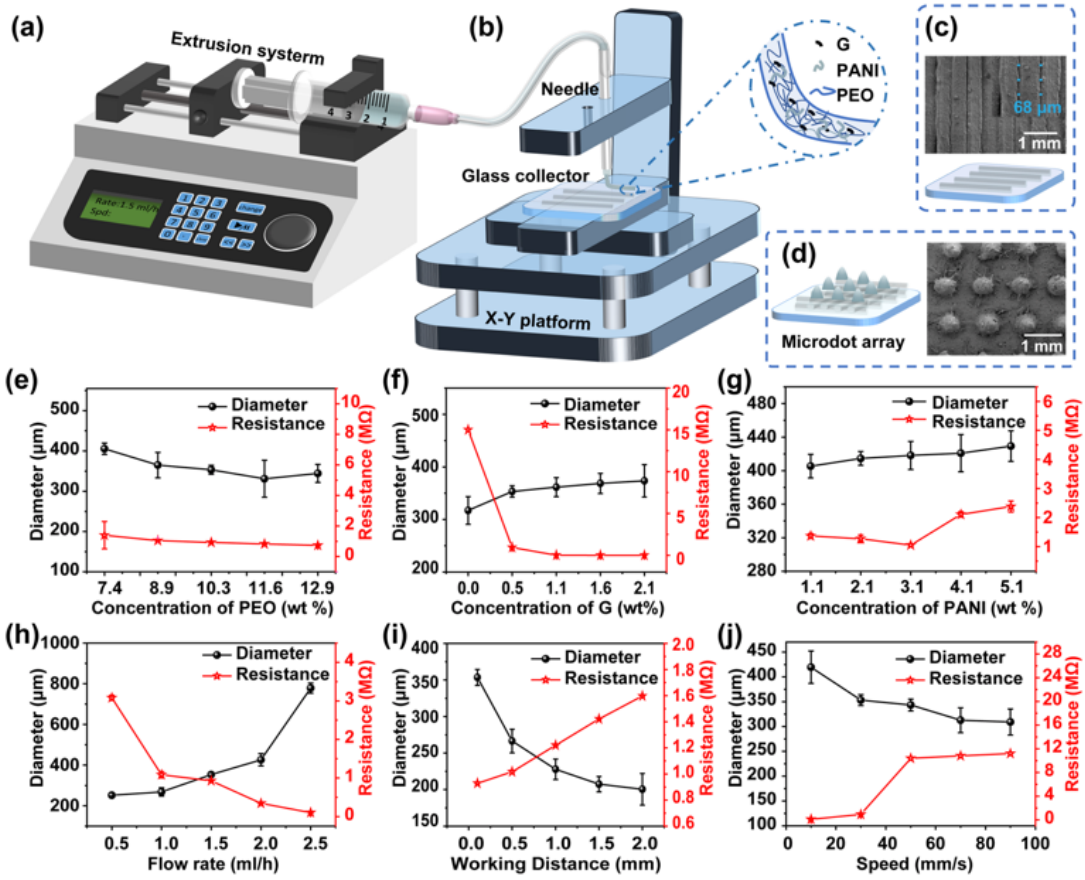

Figure 1. Direct-ink writing (DIW) of a graphene-based sensor with a conical microdot array (GSCA) and evaluation of process parameters. (a) Extrusion system for the solution (PEO/PANI/G). (b) Setup for DIW printing. (c) SEM and a sketch of the printed sensing filaments. (d) SEM and a sketch of the printed graphene-based sensing film with conical microdots; The influence on diameter and resistance of prined filament caused by the concentration of PEO (e), the concentration of G (f), the concentration of PANI (g), the flow rate (h), the working distance from the needle to the collector (i), and the platform speed (j).

Figure 1h-j indicates that the resistance changes have opposite tendencies to diameter changes with an increase in flow rate (Figure 1h), working distance (Figure 1i), and

platform speed (Figure 1j). Figure 1h indicates that the faster flow rates of the extrusion system from 0.5 to 2.5 ml/h result in more ink volume and slower volatilization speed, giving rise to a thicker diameter and better conductivity correspondingly. When the working distance increased from 0 to 2.0 mm, the extrusion ink had enough time to volatilize and be pulled by gravity, causing a thinner diameter and higher resistance. Increasing the platform speed in a gradient from 10 to 100 mm/s resulted in a relatively smaller amount of ink being extruded onto the collector, and the newly printed filament ink had more time to volatilize, thus resulting in a thinner diameter and higher resistance. According to these results, diameters in the range of 200 to 779 μm with resistances varied from 1 MΩ to infinite can be selected at appropriate values to prepare sensing ink and customize sensing film with desired properties. Considering the working efficiency, fiber diameter, and resistance, ultimately, 10.3 wt% PEO, 1.6 wt% PANI, 1.1 wt% G, 2.0 ml/h extrusion rate, 50 mm/s platform speed, and 0.1 mm working distance were chosen in this study.

3.2 Characterization

Attenuated total reflectance Fourier transform infrared spectroscopy (ATR-FTIR) and energy-dispersive X-ray spectroscopy (EDS) were used to confirm the composition, interactions, and material stability of the graphene-based sensing film (PEO/PANI/G). The effects of PANI concentrations ranging from 1.1 to 5.1 wt% on the sensing film were also studied. In Figure 2a, the characteristic peak of G is not prominent, which is consistent with previous findings.[26, 27] The characteristic peaks of PANI, which indicate the C=C stretching vibration of benzenoid and quinoid rings, occur at 1484 and 1537 cm^{-1}, respectively. [28-30] The spectra of the sensing film (PEO/PANI/G) with different PANI concentrations show the C-O-C vibration mode at 1099 cm^{-1} and the C=C stretching vibration of benzenoid and quinoid rings at 1484 and 1537 cm^{-1}, respectively. [31] These findings suggest that PANI is stable and successfully embedded into the polymeric matrix. Moreover, with the increasing concentration of PANI, the typical peaks of alkyl stretching groups (light green area) and C-O-C (lilac area) of the compound (PEO/PANI/G) gradually shift to the left because of the stronger enhanced

π-π conjugated stacked interactions between G and PANI, [25, 32] which weaken the force of a double bond and induce a redshift phenomenon. Additionally, PEO may also have an interaction with PANI, which is consistent with previous research.[33]

The composition of the elements is further supported by the EDS analysis in Figure 2b. The element C belongs to PEO and G, while O is from PEO and PANI. N is attributed to PANI, and S is due to the presence of PANI, which contains agents such as camphorsulfonic acid or benzenesulfonic acid. [25, 33] In Figure S1a-d, the four elements are distributed in their corresponding SEM image (Figure S1e) of the printed PANI/PEO/G sensing film.

The morphology and structure of the printed sensing film were examined using SEM. Figure 2c shows aligned parallel filaments with rough surfaces that were stacked 10 times layer by layer. The films with microdots of 9 (Figure 2d), 18 (Figure 2e), and 27 layers (Figure 2f) exhibit similar surface morphology and size. The microdots have a conical shape with a bottom diameter of approximately 500 μm. Figure 2g displays a magnified image of the micro/nano fiber between two microdots, which presents spider-leg-like fibers varying in segment and size, containing a fiber diameter of 18 μm and tiny threads (approximately 850 nm). Due to the high viscosity of the sensing ink, spider-leg-like micro/nanofibers could be formed when the needle moved from one microdot to the adjacent one during printing. As layer numbers increased, the spider-leg-like micro/nanofibers between two dots also increased significantly. The magnified surface morphology of the spider-legs-like micro/nanofiber in Figure 2g is shown in Figure S1f. Figure S1g, which displays the bottom side of the sensing film, shows similar surface morphology to the one in Figure S1f. The rod-like substances in Figures S1f, g, and h are from pure PANI powder.[34, 35]

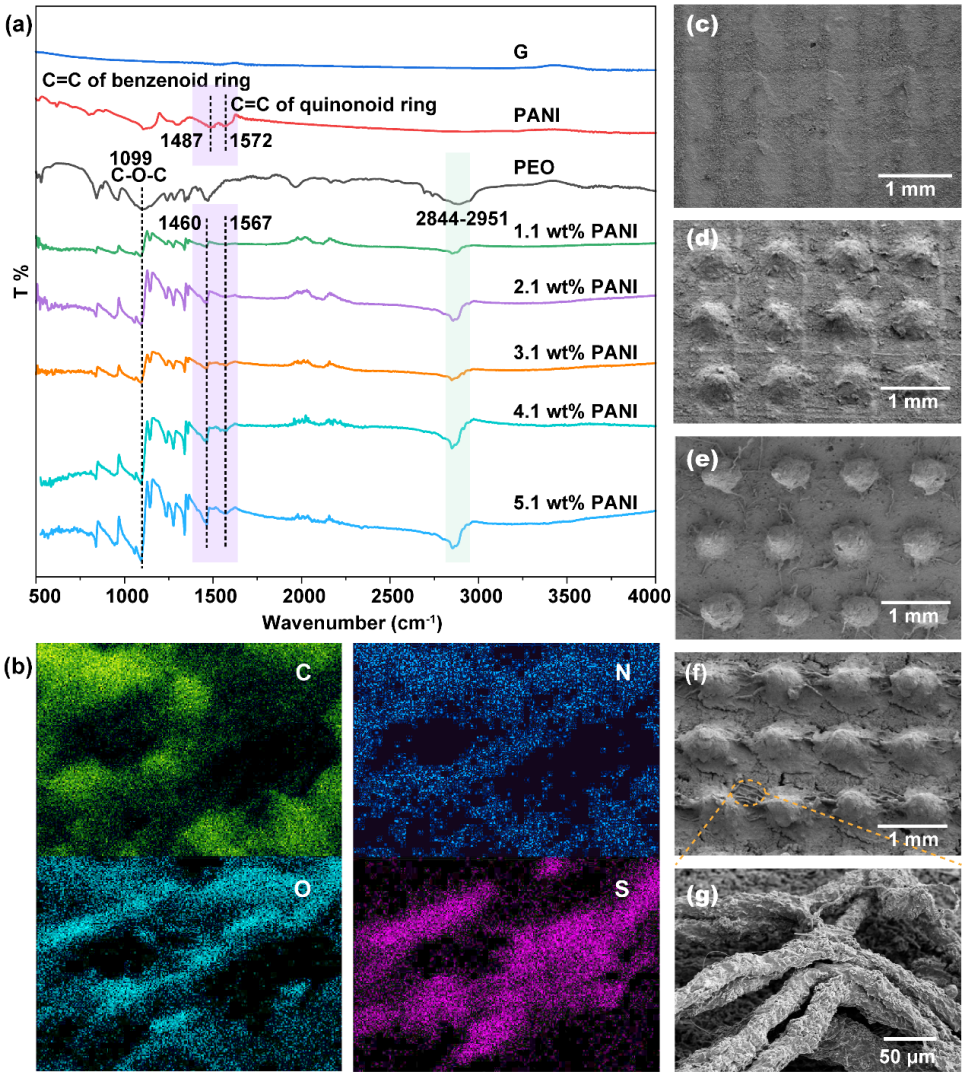

Figure 2. FTIR, EDS, and SEM results of PEO/PANI/G printed sensing film. (a) The FTIR spectrum of pure materials and PEO/PANI/G sensing film printed at different PANI concentrations (1.1-5.1 wt%). (b) The EDS results of printed PEO/PANI/G sensing film. (c) The PEO/PANI/G sensing film printed using DIW. (d-f) SEM images of PEO/PANI/G sensing film with conical microdots prepared at 9 (d), 18 (e), and 27 (f) layers. (g) Magnified SEM image of the spider-legs-like micro/nanofibers in Figure 2f.

3.3 The piezoresistive mechanism of GSCA

To understand the resistive response of the printed sensor, two simple schematics were developed to explain the working principle and a basic circuit model. Figure 3a illustrates the working mechanism of GSCA without pressure. The total resistance *R* is

composed of the constant wire resistance R_e (several ohms), the contact resistance R_c between the wires and sensing film, and the percolation resistance R_p of the sensing film with conical microdots. Regardless of whether an external pressure is applied or not, R_c has little impact on R_p, and R_e is significantly smaller than R_p. Thus, the total R can be calculated using the formula (2).

$$R_{total} = R_e + R_c + R_p \approx R_p \quad (2)$$

When an external pressure is applied, *Rp* undergoes significant changes. When pressure within a low range is applied, the microdots tend to expand in two directions (shown by the lilac arrows in Figure 3b), causing hindrance to the quantum tunneling effect of G. Consequently, an increase in the total resistance is expected. As the applied pressure increases, new conductive pathways are established under high pressure, facilitating electron conduction in sensing, and thus, the resistance is expected to decrease slightly. [36] However, a few microcracks (indicated by red curves) will be produced, and the distances between conductive additives will also increase greatly. As a result, the main cause of the increased resistance *Rp* of the sensor is due to the microcracks (as mentioned in reference. [37]

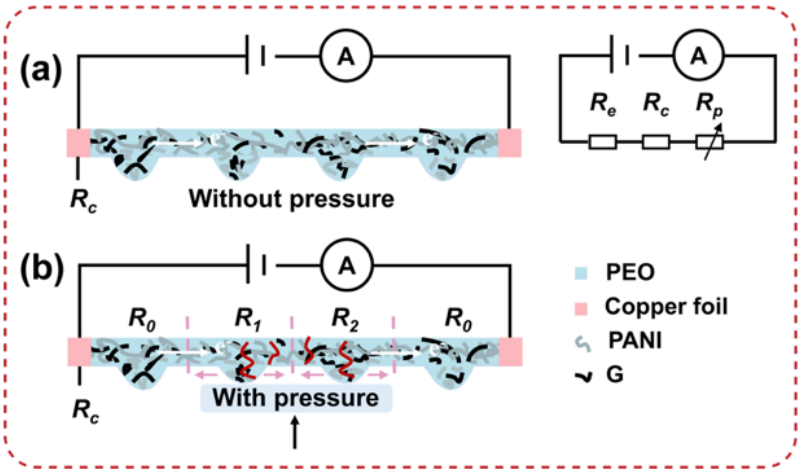

Figure 3. Basic working principle and electromechanical performance of GSCA. Schematic illustration of the working principle of GSCA without (a) and with (b) external pressure.

3.4 Electromechanical performance of GSCA

In Figure 4a, both the sensor with 27 layers and the sensor with 0 layers of microdots exhibit two linear regions of sensitivity. It should be noted that the minimum pressure applied during the sensitivity testing in Figure 4a is approximately 26 kPa. The sensor without microdots has a sensitivity of 0.034 kPa^{-1} in the first linear region (26-78 kPa, S1), and a sensitivity of 0.005 kPa^{-1} in the second linear region (78-160 kPa, S2). By introducing 27 layered microdots, the sensitivity of the printed sensor is enhanced to 0.045 kPa^{-1} (1.4-102 kPa, S3). As detailed in Figure S2a, the GSCA has a large detection range of 1.4-509 kPa, with a sensitivity of S3=0.045 kPa^{-1} and S4=0.035 kPa^{-1} (102-509 kPa). With an increase in the number of layers from 9, 18 to 27, the sensitivities of the GSCA are also enhanced, as shown in Figure S2b. Figure 4b displays good Ohmic conductive behavior of the GSCA, which agrees with previous studies. [38-40] The slopes of the curves keep decreasing when the pressure increases from 0 to 45.4 kPa, exhibiting positive piezoresistive behavior. Figure 4c displays the relative resistance change at three pressure scales, demonstrating the stability and fast response of the sensor. Figure 4d shows that the outputs remain around 21% at every 100 cycles in the total 1000 cycles under a cyclic pressure of 95.5 kPa. Figure 4e shows that the signal change caused by a static pressure of 11.4 Pa can also be detected, with a corresponding response time of 60 ms. However, the recovery time is relatively long due to the intrinsic hysteresis property of the polymer. Figure 4f confirms the slight stress relaxation and hysteresis properties under loaded and unloaded pressure. The slight stress relaxation property is inherent to polymers and has almost no effect on the response time and outputs in this work. When unloading pressure, the response signal has a 512 ms delay because the breaking speed of the established conductive paths is much higher than the recovery speed of cracks in the polymeric sensing film.

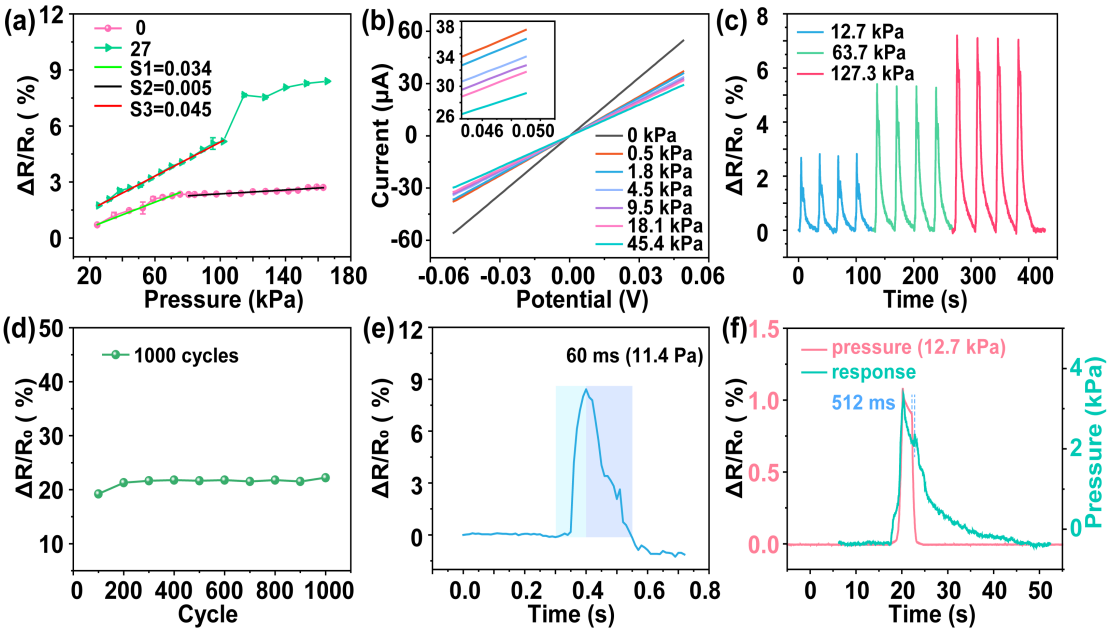

Figure 4. Electromechanical performance analysis of GSCA. (a) Dynamic resistance response of the printed sensor with and without 27 layered microdots under pressure. The red line shows the linear fitting for calculating the sensitivity of GSCA with 27 layered microdots, while the light green line shows the sensitivity of GSCA without microdots. (b) Current-voltage (I-V) curve of GSCA under various applied pressures. (c) Relative resistance changes of GSCA upon three different applied cyclic forces. (d) Stability of GSCA under 1000 loading-unloading cycles at a mechanical speed of 10 mm/min. (e) Response and recovery times of GSCA under an applied pressure of 11.4 Pa. (f) Relative resistance changes (green) and pressure changes (pink) over time.

3.5 Applications of GSCA

Figure 5a shows the GSCA placed on the wrist of a female to detect real-time pulse beats. The results show a pulse rate of approximately 68 beats per minute. The detailed signal, marked with a black rectangular dotted line, is displayed in Figure S3a. Three wave components, including the percussion (P1) wave, tidal wave (P2), and diastolic wave (P3), can be observed, indicating good sensitivity and signal-to-noise ratio of the GSCA. Therefore, the printed GSCA shows potential for healthcare monitoring, especially for those suffering from asthma, cardiovascular, or heart disease. Figure 5b

illustrates decoding the Morse code "CNS." The sensor shows potential as a medium for Morse code decoding and can be coated onto surfaces to acquire necessary confidential information. When applied with instantaneous pressure, the output of the GSCA shows only one response peak, while applied with pressure lasting for a few seconds, the output shows one response and one recovery peak.

Normal human respiration also exhibits a "two peaks" response in Figure 5c detected by a GSCA embedded in a commercial mask. The pressure induced by expiratory air causes the deformation of the GSCA, and then the change in signals can be detected. The respiratory rate can be easily calculated using the number of peaks, and the breath intensity can be characterized by the amplitude of the peaks when breathing occurs. Thus, the sensor can potentially be used to monitor breathing frequency and strength for patient diagnosis at home or in the hospital. The GSCA can also be used to detect airflow pressure produced by a rubber suction bulb in our research. The rubber suction bulb was placed 1 cm above the GSCA and was squeezed with different forces to produce air pressure. The sensor shows good responses to air pressure induced by airflow, as shown in Figure 5d.

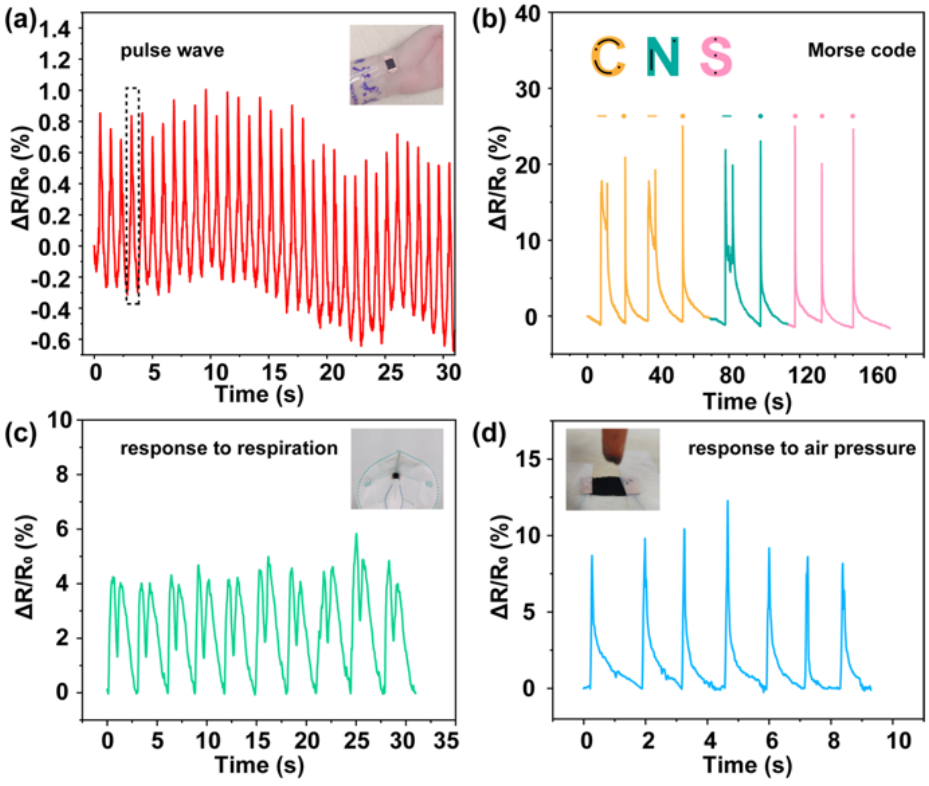

Figure 5. Applications of the fully printed GSCA. (a) Real-time pulse monitoring on the wrist. (b) Decoding Morse code by knocking on the GSCA. The Morse code for "C N S" is marked with black dots and curves in the inserted letters. (c) Human breath monitoring using a commercial mask. (d) Response to air pressure produced by a rubber suction bulb.

3.6 Aircouplant detection using GSCA

It is well known that most flexible sensors need to be attached to human skin to monitor human motion, which limits their applications in various scenarios. However, the fast response of GSCA to aircouplant detection makes it promising to monitor multiscale and multi-angle airflow without touching the human skin. To explore the performance of GSCA as an aircouplant sensor, we measured the resistance variation in response to airflow under various conditions. Figure 6a shows the measurement of airflow with various aeration rates and directions using an air tank with a flow outlet at different angles (θ), where θ is defined as the angle between the directions of airflow and the y-axis. When the direction of airflow is parallel to the y-axis, the angle θ is 0°.

In Figure 6b, the airflow from different directions is decomposed into directions of the x and y-axis. When θ equals 0° or 90°, the GSCA is mainly affected by airflow from a single direction, whereas at 45°, the sensor receives airflow from two directions (x and y). We compared the relative resistance variations in Figure 6c-e under the same aeration rates. The output response of θ at 0° is slightly less than the results of θ at 90°, and both changes are smaller than the results of θ at 45°. The detailed values are shown in Table S1 in the supporting information. Moreover, the peak shapes at different aeration rates are similar, and the amplitude of the response curves increases as the aeration rates increase from 2 to 8 L/min. Interestingly, as the aeration rate increases, the relative resistance variation also enhances linearly at three different angles, as shown in Figure S4a. Similarly, when the aeration rate is fixed, the angle of airflow can also be identified according to the results in Figure S4b. Therefore, the printed GSCA shows good sensitivity and quick response to air strength induced by various aeration

rates. Based on these results, the printed GSCA shows high sensitivity to recognize the direction and intensity of airflow and has the potential to be used as an aircouplant sensor for airflow indicators.

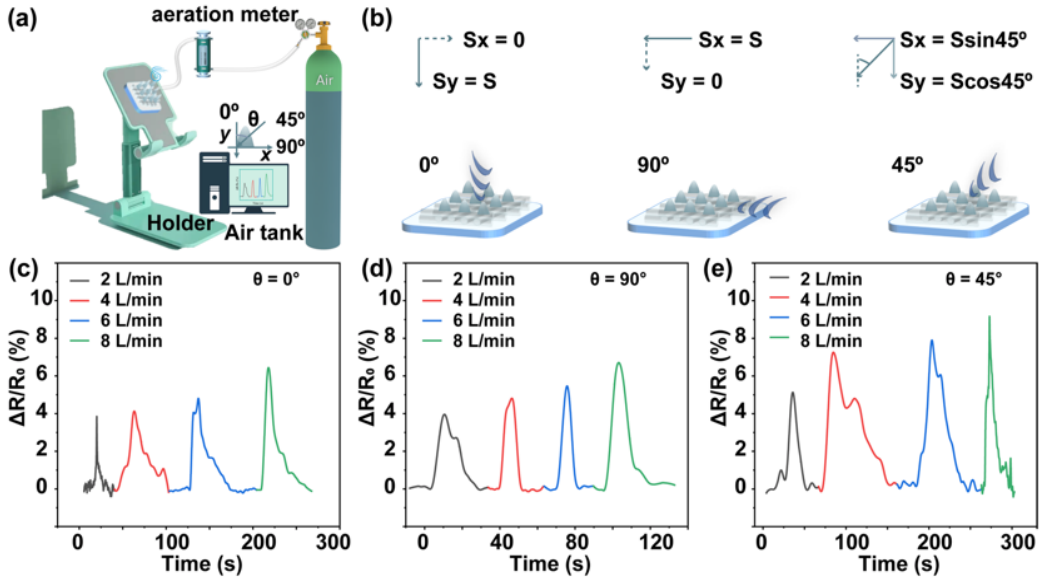

Figure 6. Airflow detection using GSCA. (a) Schematic diagram of the device used for the airflow sensing test. θ represents the angle between the direction of airflow and the y-axis. (b) Schematic analysis of GSCA subjected to airflow at different angles. (c-e) Relative resistance changes versus time at different aeration rates and angles: 0° (c), 90° (d), and 45° (e).

4. Conclusion

In conclusion, the direct-ink writing (DIW) method has been used to achieve a graphene-based flexible sensor with a conical microdot array (GSCA) for wearable and airflow monitoring. The study found that the concentrations of PEO/PANI/G, flow rate, platform speed, and working distance significantly affect the resistance and diameter of sensing filaments. Optimized processing parameters can be used to customize structures and improve the sensitivity of the GSCA. The strong π-π stacking force between PANI and G contributes to high conductivity and good sensitivity. The fabricated sensor with 27 layered microdots showed a positive piezoresistive effect and

improved sensitivities of 32.4% (26-78 kPa), 800% (78-102 kPa), and 600% (102-160 kPa) compared to the sensor without microdots. The GSCA exhibits a large detection range (1.4-509 kPa), low detection limit (11.4 Pa), fast response (60 ms), and good durability. It has been demonstrated that the GSCA is a good candidate for precision monitoring of pulse waves, respiration, and Morse code. The sensor can also distinguish transient from steady pressure based on the peak numbers under one stimulation. Finally, the DIW-printed CAGS has been shown to have the ability to recognize airflow strength and direction for aircouplant applications.

Declaration of Competing Interest

The authors declare that they have no known competing financial interests or personal relationships that could have appeared to influence the work reported in this paper.

Acknowledgement

The authors sincerely acknowledge financial support from the National Natural Science Foundation of China (No. 81771960 to M.W.C), National Natural Science Foundation of China (No. 82172064 to X.C.), Major Scientific Project of Zhejiang Lab (No. 2020MC0AD01 to X.C.), the National Key Research and Development Program of China (No. 2019YFC1711800 to J.L.), and the Pioneer Project of Zhejiang province (No. 2022c03188 to X.C.). Informed consent was obtained from all volunteers who participated in this study.

Supporting Information

The supplementary results for EDS, SEM, electromechanical performance, and applications in pulse wave, respiration detection, and airflow detection are included. A table is also provided that shows the relative resistance changes caused by different airflow speeds and angles.

References

1. Shohag, M. A. S.; Eze, V. O.; Braga Carani, L.; Okoli, O. I., Fully Integrated Mechanoluminescent Devices with Nanometer-Thick Perovskite Film as Self-Powered Flexible Sensor for Dynamic Pressure Sensing. *ACS Appl. Nano Mater.* **2020,** *3* (7), 6749-6756.

2. Zhang, G. H.; Zhang, L.; Zhu, Q. H.; Chen, H.; Yuan, W. L.; Fu, J.; Wang, S. L.; He, L.; Tao, G. H., Self-Healable, Malleable, and Flexible Ionic Polyimine as an Environmental Sensor for Portable Exogenous Pollutant Detection. *ACS Mater. Lett.* **2022,** *4* (1), 136-144.

3. Dai, C. L.; Liu, M. C.; Chen, F. S.; Wu, C. C.; Chang, M. W., A nanowire WO3 humidity sensor integrated with micro-heater and inverting amplifier circuit on chip manufactured using CMOS-MEMS technique. *Sens. Actuators B Chem.* **2007,** *123* (2), 896-901.

4. Bartolozzi, C.; Natale, L.; Nori, F.; Metta, G., Robots with a sense of touch. *Nat. Mater.* **2016,** *15* (9), 921-925.

5. Wang, H.; Totaro, M.; Beccai, L., Toward Perceptive Soft Robots: Progress and Challenges. *Adv. Sci.* **2018,** *5* (9), 1800541.

6. Osborn, L. E.; Dragomir, A.; Betthauser, J. L.; Hunt, C. L.; Nguyen, H. H.; Kaliki, R. R.; Thakor, N. V., Prosthesis with neuromorphic multilayered e-dermis perceives touch and pain. *Sci. Robot.* **2018,** *3* (19), eaat3818.

7. Yang, J. C.; Mun, J.; Kwon, S. Y.; Park, S.; Bao, Z.; Park, S., Electronic Skin: Recent Progress and Future Prospects for Skin-Attachable Devices for Health Monitoring, Robotics, and Prosthetics. *Adv. Mater.* **2019,** *31* (48), 1904765.

8. Tang, G.; Shi, Q.; Zhang, Z.; He, T.; Sun, Z.; Lee, C., Hybridized wearable patch as a multi-parameter and multi-functional human-machine interface. *Nano Energy* **2021,** *81*, 105582.

9. Guo, Y.; Guo, Z.; Zhong, M.; Wan, P.; Zhang, W.; Zhang, L., A Flexible Wearable Pressure Sensor with Bioinspired Microcrack and Interlocking for Full-Range Human - Machine Interfacing. *Small* **2018,** *14* (44), 1803018.

10. Zhai, W.; Xia, Q.; Zhou, K.; Yue, X.; Ren, M.; Zheng, G.; Dai, K.; Liu, C.; Shen, C., Multifunctional flexible carbon black/polydimethylsiloxane piezoresistive sensor with ultrahigh linear range, excellent durability and oil/water separation capability. *Chem. Eng. J.* **2019,** *372*, 373-382.

11. Wang, C. Y.; Xia, K. L.; Wang, H. M.; Liang, X. P.; Yin, Z.; Zhang, Y. Y., Advanced Carbon for Flexible and Wearable Electronics. *Adv. Mater.* **2019,** *31* (9), 1801072.

12. Lin, J. X.; Hu, H. W.; Luo, J.; Miao, L.; Yang, Z. H.; Chen, M.; Zhang, M.; Ou, J. Z., Micro/nanoarrays and their applications in flexible sensors: A review. *Mater. Today Bio.* **2022,** *19*, 100224.

13. Cheng, B. C.; Wu, P. Y., Scalable Fabrication of Kevlar/Ti3C2Tx MXene Intelligent Wearable Fabrics with Multiple Sensory Capabilities. *ACS Nano* **2021,** *15* (5), 8676-8685.

14. Meena, J. S.; Choi, S. B.; Jung, S. B.; Kim, J. W., Recent progress of Ti3C2Tx-based MXenes for fabrication of multifunctional smart textiles. *Appl. Mater. Today* **2022,** *29*, 101612.

15. Yu, Q.; Jiang, J.; Su, C.; Huang, Y.; Chen, N.; Shao, H., Ti3C2Tx MXene/polyvinyl alcohol decorated polyester warp knitting fabric for flexible wearable strain sensors. *Text. Res. J.* **2021,** *92* (5-6), 810-824.

16. Zhang, J.; Li, J.; Cheng, W.; Zhang, J.-H.; Zhou, Z.; Sun, X.; Li, L.; Liang, J.-G.; Shi, Y.; Pan, L., Challenges in Materials and Devices of Electronic Skin. *ACS Mater. Lett.* **2022,** *4* (4), 577-599.

17. Sun, R.; Wang, B.; Zhang, L.; Lang, Y.; Chang, M.-W., Engineering Three-Dimensional Bendable Helix Conduits for Peripheral Nerve Regeneration via Hybrid Electrotechnologies. *ACS Mater. Lett.* **2022,** *4* (11), 2210-2218.

18. Chen, B.; Jiang, Y.; Tang, X.; Pan, Y.; Hu, S., Fully Packaged Carbon Nanotube Supercapacitors by Direct Ink Writing on Flexible Substrates. *ACS Appl. Mater. Interfaces* **2017,** *9* (34), 28433-28440.

19. Wang, B. L.; Ahmad, Z.; Huang, J.; Li, J. S.; Chang, M. W., Development of random and ordered composite fiber hybrid technologies for controlled release functions. *Chem. Eng. J.* **2018,** *343*, 379-389.

20. Huang, K.; Dong, S.; Yang, J.; Yan, J.; Xue, Y.; You, X.; Hu, J.; Gao, L.; Zhang, X.; Ding, Y., Three-dimensional printing of a tunable graphene-based elastomer for strain sensors with ultrahigh sensitivity. *Carbon* **2019,** *143*, 63-72.

21. Shi, G.; Lowe, S. E.; Teo, A. J. T.; Dinh, T. K.; Tan, S. H.; Qin, J.; Zhang, Y.; Zhong, Y. L.; Zhao, H., A versatile PDMS submicrobead/graphene oxide nanocomposite ink for the direct ink writing of wearable micron-scale tactile sensors. *Appl. Mater. Today* **2019,** *16*, 482-492.

22. Wang, Z.; Zhang, Q. e.; Long, S.; Luo, Y.; Yu, P.; Tan, Z.; Bai, J.; Qu, B.; Yang, Y.; Shi, J.; Zhou, H.; Xiao, Z.-Y.; Hong, W.; Bai, H., Three-Dimensional Printing of Polyaniline/Reduced Graphene Oxide Composite for High-Performance Planar Supercapacitor. *ACS Appl. Mater. Interfaces* **2018,** *10* (12), 10437-10444.

23. Zhao, J.; Zhang, Y.; Zhao, X.; Wang, R.; Xie, J.; Yang, C.; Wang, J.; Zhang, Q.; Li, L.; Lu, C.; Yao, Y., Direct Ink Writing of Adjustable Electrochemical Energy Storage Device with High Gravimetric Energy Densities. *Adv. Funct. Mater.* **2019,** *29* (26), 1900809.

24. Zhang, Y.; Shi, G.; Qin, J.; Lowe, S. E.; Zhang, S.; Zhao, H.; Zhong, Y. L., Recent Progress of Direct Ink Writing of Electronic Components for Advanced Wearable Devices. *ACS Appl. Electron. Mater.* **2019,** *1* (9), 1718-1734.

25. Cho, S.; Lee, J. S.; Jun, J.; Kim, S. G.; Jang, J., Fabrication of water-dispersible and highly conductive PSS-doped PANI/graphene nanocomposites using a high-molecular weight PSS dopant and their application in H2S detection. *Nanoscale* **2014,** *6* (24), 15181-95.

26. Wang, B. L.; Chen, X.; Ahmad, Z.; Huang, J.; Chang, M. W., 3D electrohydrodynamic printing of highly aligned dual-core graphene composite matrices. *Carbon* **2019,** *153*, 285-297.

27. Song, Y. H.; Dong, H.; Liu, W. X.; Fu, X.; Fu, Z.; Li, P. L.; Chen, L.; Ahmad, Z.; Liu, J.; Chen, X.; Chang, M. W., Electrostatic Jet Engineering of Flexible Composite Pressure Sensors for Physical Applications. *ACS Appl. Polym. Mater.* **2022,** *4* (2), 868-878.

28. Chang, C. M.; Weng, C. J.; Chien, C. M.; Chuang, T. L.; Lee, T. Y.; Yeh, J. M.; Wei, Y., Polyaniline/carbon nanotube nanocomposite electrodes with biomimetic hierarchical structure for supercapacitors. *J. Mater. Chem. A* **2013,** *1* (46), 14719-14728.

29. Wang, Y.; Gao, X.; Fu, Y.; Wu, X.; Wang, Q.; Zhang, W.; Luo, C., Enhanced microwave absorption performances of polyaniline/graphene aerogel by covalent bonding. *Compos. B. Eng.* **2019,** *169*, 221-228.

30. Simotwo, S. K.; DelRe, C.; Kalra, V., Supercapacitor Electrodes Based on High-Purity Electrospun Polyaniline and Polyaniline-Carbon Nanotube Nanofibers. *ACS Appl. Mater. Interfaces* **2016,** *8* (33), 21261-9.

31. Aliabadi, M.; Irani, M.; Ismaeili, J.; Piri, H.; Parnian, M. J., Electrospun nanofiber membrane of PEO/Chitosan for the adsorption of nickel, cadmium, lead and copper ions from aqueous solution. *Chem. Eng. J.* **2013,** *220*, 237-243.

32. Shin, K. Y.; Cho, S.; Jang, J., Graphene/polyaniline/poly(4-styrenesulfonate) hybrid film with uniform surface resistance and its flexible dipole tag antenna application. *Small* **2013,** *9* (22), 3792-8.

33. Duan, Y.; Tang, Q.; Chen, Y.; Zhao, Z.; Lv, Y.; Hou, M.; Yang, P.; He, B.; Yu, L., Solid-state dye-sensitized solar cells from poly(ethylene oxide)/polyaniline electrolytes with catalytic and hole-transporting characteristics. *J. Mater. Chem. A* **2015,** *3* (10), 5368-5374.

34. Eskizeybek, V.; Sarı, F.; Gülce, H.; Gülce, A.; Avcı, A., Preparation of the new polyaniline/ZnO nanocomposite and its photocatalytic activity for degradation of methylene blue and malachite green dyes under UV and natural sun lights irradiations. *Appl. Catal., B* **2012,** *119-120*, 197-206.

35. Wu, Z.; Chen, X.; Zhu, S.; Zhou, Z.; Yao, Y.; Quan, W.; Liu, B., Enhanced sensitivity of ammonia sensor using graphene/polyaniline nanocomposite. *Sens. Actuators B Chem.* **2013,** *178*, 485-493.

36. Zhao, B.; Zhang, X.; Deng, J.; Zhang, C.; Li, Y.; Guo, X.; Zhang, R., Flexible PEBAX/graphene electromagnetic shielding composite films with a negative pressure effect of resistance for pressure sensors applications. *RSC Adv.* **2020,** *10* (3), 1535-1543.

37. Wang, Y. F.; Sekine, T.; Takeda, Y.; Hong, J.; Yoshida, A.; Matsui, H.; Kumaki, D.; Nishikawa, T.; Shiba, T.; Sunaga, T.; Tokito, S., Printed Strain Sensor with High Sensitivity and Wide Working Range Using a Novel Brittle - Stretchable Conductive Network. *ACS Appl. Mater. Interfaces* **2020,** *12* (31), 35282-35290.

38. Tian, K.; Sui, G.; Yang, P.; Deng, H.; Fu, Q., Ultrasensitive Thin-Film Pressure Sensors with a Broad Dynamic Response Range and Excellent Versatility Toward Pressure, Vibration, Bending, and Temperature. *ACS Appl. Mater. Interfaces* **2020,** *12* (18), 20998-21008.

39. Kim, K.; Jung, M.; Kim, B.; Kim, J.; Shin, K.; Kwon, O.-S.; Jeon, S., Low-voltage, high-sensitivity and high-reliability bimodal sensor array with fully inkjet-printed flexible conducting electrode for low power consumption electronic skin. *Nano Energy* **2017,** *41*, 301-307.

40. Zhu, B.; Niu, Z.; Wang, H.; Leow, W. R.; Wang, H.; Li, Y.; Zheng, L.; Wei, J.; Huo, F.; Chen, X., Microstructured Graphene Arrays for Highly Sensitive Flexible Tactile Sensors. *Small* **2014,** *10* (18), 3625-3631.